Smart Structures and Systems, *Vol. 28, No. 4 (2021) 567-578*
https://doi.org/10.12989/sss.2021.28.4.567

A hybrid nondestructive testing method for detecting cavities behind the retaining wall

Jung-Doung Yu [1a], Jong-Sub Lee [1b] and Hyun-Ki Kim*[2]

[1] *School of Civil, Environmental, and Architectural Engineering, Korea University, 145 Anam-ro, Seongbuk-gu, Seoul 02841, Republic of Korea*
[2] *Department of Civil and Environmental Engineering, Kookmin University, 77 Jeongneung-ro, Seongbuk-gu, Seoul 02707, Republic of Korea*

(*Received February 10, 2021, Revised September 3, 2021, Accepted September 6, 2021*)

Abstract. This study proposes a combination of nondestructive testing methods for detecting soil cavities behind retaining walls, which adversely affect the stability of the sloping ground or retaining structures. An experimental study is conducted using a soil chamber filled with dry sands retained by a concrete wall plate. A hemispherical soil cavity is simulated just behind the wall plate, and elastic wave reflections of impacts on the wall are measured using accelerometers. The measured elastic waves are analyzed using the signal energy in time domain and predominant frequency and mobility spectrum in frequency domain. In addition, spatiotemporal changes in the surface of the wall during heating and cooling sequences are monitored using infrared thermography. The captured thermal image is then used for identifying the cavity. Experimental results show that the cavity leads to increases in the signal energy, predominant frequency, and flexibility in the mobility spectrum. The contrasts in the thermal images effectively reveal the shapes and locations of the soil cavity. This study demonstrates that the hybrid testing method that conducts a careful inspection by elastic waves on areas suspected in the preliminary scanning by the infrared thermography can be competitive and effective for detecting soil cavities.

Keywords: cavity detection; elastic wave; nondestructive evaluation; retaining wall; thermal image

1. Introduction

A retaining wall is a structure used in geotechnical engineering to resist lateral earth pressure generated by back soils, liquids, or other materials in areas of abrupt changes in ground elevation such as ground excavation sites, embankments, and soil slopes (Brooks 2010, Ching and Winkel 2018). Retaining walls are typically designed to consider the unit weight, strength properties, and groundwater conditions of the backfill materials as well as lateral earth pressure. Backfill materials with high permeability are typically used to minimize the lateral earth pressure exerted on the wall by groundwater (Obe *et al*. 2017, Yang *et al*. 2019); those with low permeability cause water accumulation behind the retaining wall. This phenomenon increases the lateral earth pressure applied on the wall, which results in cracks or structural deformation. Thus, proper structural design for bearing lateral earth pressure and appropriate backfill materials for providing proper drainage are important to ensure stability in the structures, ground, and slopes. However, numerous retaining wall failures through poor design or substandard construction combined with heavy rainfall have been reported (Koerner and Soong 2001, Padhye and Ullagaddi 2008, Prasad *et al*. 2014, Yoo and Jung 2006). Furthermore, social concern about retaining wall failures caused by deterioration has recently increased. Such deterioration reduces the durability of the retaining wall under freeze–thaw cycles, which leads to discoloration, erosion, delamination, cracking, and eventual disintegration of the retaining wall (Embacher *et al*. 2001). Wall deterioration can generate cavities behind the wall, which enable backfill materials, retained soils, and groundwater to breach the wall. Moreover, if the drainage pipe of the retaining wall is damaged by deterioration, these materials can infiltrate the drainage pipe through cavity generation. These problems can be exacerbated by rainfall. The cavities behind the wall can cause ground settling and the collapse of structures on the ground. Thus, the cavities generated behind the retaining wall should be inspected to prevent disasters.

During the last 10 years, numerous attempts have been made to inspect the structural health of retaining walls using nondestructive evaluation (NDE) techniques. Hugenschmidt and Kalogeropoulos (2009) used ground-penetrating radar (GPR) to inspect retaining walls by investigating the locations of rebars in the walls. Shinoda *et al*. (2013) performed experimental studies using a model retaining wall with a height of 1 m. In their research, the vibration characteristics of the retaining wall was investigated, and the area of the amplitude in the Fourier spectrum was used as an index for evaluating the deformation degree in the wall. Rainieri *et al*. (2013) conducted field experiments for

*Corresponding author, Ph.D., Professor,
E-mail: geotech@kookmin.ac.kr
[a] Ph.D., Research Professor
[b] Ph.D., Professor

ISSN: 1738-1584 (Print), 1738-1991 (Online)

monitoring the seismic responses of retaining walls of various elevations. In their studies, ambient vibrations were measured using an accelerometer, and the results were analyzed using natural frequency and modal displacement considering the wall elevation differences. Recently, Lin *et al*. (2019) introduced a dynamic imaging system to detect cracks of retaining walls. A charge-coupled device (CCD) camera was equipped on a drone and surfaces of retaining walls were scanned and then types of cracks were analyzed using the machine vision correlation algorithm. Although the CCD camera provides high resolution information and effectively detects cracks, its high battery consumption prevents long-time monitoring. Seo *et al*. (2019) used 3D laser scanners for monitoring the structural displacement of the retaining wall. Laser scanner provided high spatial resolution. However, the measurement accuracy was low. Thus, it is not sufficient for daily monitoring of the displacement but is suitable for monitoring cumulative change. Such previous studies have realized considerable achievements in the structural health monitoring of retaining walls; however, few studies have attempted to inspect the cavities present behind retaining walls.

The effectiveness of elastic waves has been proved theoretically and experimentally in the local detection of underground cavities. In addition, thermal imaging is a promising non-contact technology that can convert temperature information of the surface of a concrete wall into an image over a large area. The objective of the present study is to investigate suitability of elastic waves and thermal imaging for detecting cavities in backfill materials or soils accumulated behind retaining walls. Experimental studies are conducted on a small-scale retaining wall composed of a concrete plate behind which soils are accumulated. A cavity is artificially simulated in the soils using a hemispherical-shaped plastic form. In the experiments, the elastic waves are generated using a hammer impact and are measured using an accelerometer. The measured elastic waves are then analyzed using signal energy, area under the curve (AUC) of the fast Fourier transform (FFT), predominant frequency, and flexibility in the mobility spectrum. In addition, an infrared thermal image of the concrete plate is captured during heating and cooling of the plate. Then, the shape and location of the cavity is identified by comparing thermal images that vary with temperature. The remainder of this paper includes the theoretical background of the study in section 2, experimental studies in section 3, experimental results in section 4, analyses and discussions in section 5, and the summary and conclusions in section 6.

2. Theoretical background

2.1 Signal energy

Impact from a hammer applied to a concrete plate in free space generates elastic waves that propagate in the plate. Multiple reflections of elastic waves consequently occur in the concrete plate owing to the impedance mismatch between the plate and air. In this case, the energy of the elastic waves is trapped within the concrete plate; hence, the energy attenuation is small. However, if the concrete plate supports soils, a significant portion of the energy is transmitted into the soils, and the remainder is reflected back into the concrete plate. Thus, the energy of elastic waves measured at a point on the concrete plate behind which a cavity is present will be greater than that measured without a cavity. In the present study, the elastic waves were measured using an accelerometer for conversion into acceleration signals. According to Parseval's theorem, the total energy of the measured acceleration signals can be expressed as the sum (or integral) of the square of the measured signals in the time domain, which is equal to the sum (or integral) of the square of the measured signals in frequency domain as

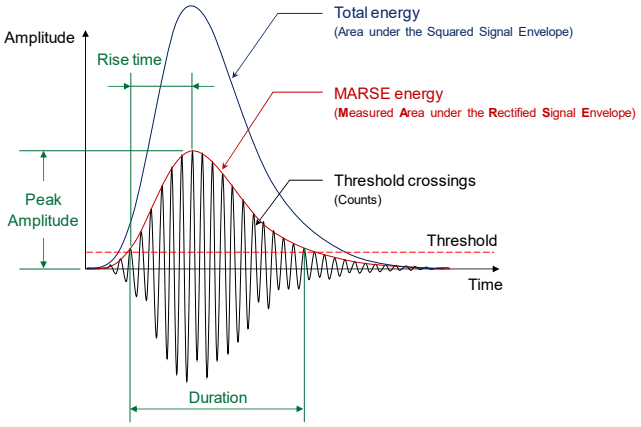

Fig. 1 Definition of terms used to characterize the signal (Unnþórsson, 2013)

$$\text{Energy}_{\text{total}} = \int_{-\infty}^{\infty} x(t)^2 dt = \int_{-\infty}^{\infty} |X(f)|^2 df, \quad (1)$$

where t and f are time and frequency, respectively; $x(t)$ represents the measured signals in the time domain; and $X(f)$ is the Fourier transform of the measured signals. The measured area under the rectified signal envelope (MARSE) energy, which is also known as the relative signal strength, is another technique used for expressing the signal energy (Grandt 2004, Unnþórsson 2013), as shown in Fig. 1. The MARSE energy is generally defined as the AUC of the measured signals above a threshold level or the AUC of the absolute value of the measured signal. In this study, the MARSE energy is calculated by integrating the absolute value of the measured signals in the time domain as

$$\text{Energy}_{\text{MARSE}} = \int_{-\infty}^{\infty} |x(t)| dt. \quad (2)$$

2.2 Flexibility in mobility spectrum

A concrete plate supporting soils that is subjected to normal excitation can be approximated as a single degree of freedom (SDOF) described by mass, spring, and dashpot (Davis and Dunn 1974, Gazetas 1993, McCavitt *et al*. 1992, Nazarian *et al*. 1994). This approximation also has been used to analyze the dynamic responses of retaining walls

supporting soils (Choudhury and Chatterjee 2006, Papazafeiropoulos *et al*. 2009, Veletsos and Younan 1994). The frequency response of the SDOF system under vibration can be expressed as a mobility spectrum in the NDE technique widely used to evaluate the integrity of concrete structures (Davis 2003, Ottosen *et al*. 2004). The mobility is defined as the transfer function between the force (F) and velocity (V); that is, it is an inverse of the impedance. The mobility can be obtained by dividing the velocity spectrum by the force spectrum as

$$\text{Mobility}(\omega) = {V(\omega)}/{F(\omega)}, \quad (3)$$

where ω is the angular frequency. The mobility plotted in the frequency domain is known as the mobility spectrum, as illustrated in Fig. 2 (ASTM C1740). In the mobility spectrum, the initial slope within 40 Hz is defined as the flexibility (or dynamic compliance) at the measurement point, expressed in units of meters per Newton. The inverse of the flexibility (i.e., the inverse of the initial slope) is known as the dynamic stiffness, expressed in units of Newtons per meter. The flexibility or dynamic stiffness at a frequency close to 0 Hz is known as static flexibility or static stiffness, respectively. In an SDOF system, which simulates the concrete plate the supporting soils, the stiffness of the spring and the damping of the dashpot are directly related to the properties of the soils supported by the concrete plate (Nazarian *et al*. 1994). Thus, the presence of the cavity decreases the stiffness of the system and hence increases the initial slope in the mobility spectrum. That is, the presence of a cavity behind the concrete plate increases the flexibility obtained from the mobility spectrum.

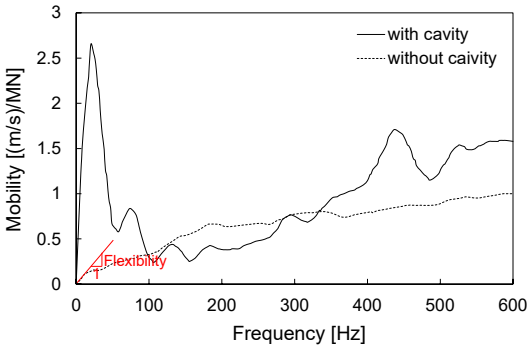

Fig. 2 Example of the mobility spectrum (ASTM C1740 2016)

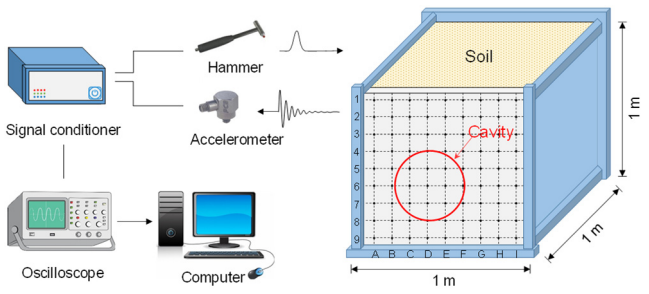

Fig. 3 Elastic wave measurement system

3. Experimental studies

3.1 Materials and methods

3.1.1 Materials

The NDE technique using elastic waves was adopted to detect cavities in backfill materials or retained soils accumulated behind the retaining walls, as shown in Fig. 3. The experiments were performed with a small-scale model of a retaining wall. The model was created by installing the concrete plate in a steel soil chamber. The model was created by installing the concrete plate in a steel soil chamber. The height, length, and depth of the soil chamber were 1 m, 1 m, and 1 m, respectively; the height, width, and thickness of the concrete plate were 90 cm, 90 cm, and 10 cm, respectively. The thickness of concrete plate was designed considering that the Korean design standard for concrete wall (KDS 14 20 72, 2021) instructs the minimum thickness of the concrete wall must be larger than 10 cm. The elastic modulus of the concrete was 36.6 GPa. A total of 81 grid points (A1–I9) were set as measurement points spaced 10 cm apart on the concrete plate, as shown in Fig. 3. An artificial cavity was simulated behind the concrete plate, the center of which was located at point D6. The cavity size was selected considering that soils are susceptible to subsidence under overburden loads if the cavity is as large as a cubic of 10 cm × 10 cm × 10 cm (Park *et al*. 2017). The cavity was produced by a plastic hemispherical-shaped form with a radius of 20 cm, which is sufficiently larger than the cavity size described above. Backfill materials supporting the concrete plate were prepared with soils composed of dry sands with 2.67 specific gravity, 0.56 mm grain size (D_{50}), and 60% relative density.

3.1.2 Elastic wave measurement

The elastic waves were generated by impacting a point located 10 mm to the right of the measurement point on the concrete plate. To produce the impact and to measure its force, an instrument hammer (086D05, PCB Piezotronics, Depew, New York, United States) weighing 5.1 N was used. A plastic hammer tip was selected to prevent unexpected noise and to measure the frequency range of interest. Elastic waves measurement was performed at all grid points using an accelerometer (353B15, PCB Piezotronics) with an operating frequency of 0.7–18 kHz and a resonance frequency of 70 kHz. The accelerometer was installed on the concrete plate using thermoplastic material (standard hot glue). A signal conditioner (482A16, PCB Piezotronics) was used for signal amplification and noise filtering. The measured signals were displayed on an oscilloscope (DSOX3014A, Keysight Technologies, Santa Rosa, California, United States) and were then recorded using a computer. Signals higher than 5 kHz were mathematically filtered. Notably, elastic waves were measured with a sampling rate of 1,000,000 samples/sec. The Nyquist frequency is therefore 0.5 MHz, which is much greater than the operating frequency (0.7–18 kHz) of the accelerometer used in the study. Thus, the resulting discrete-time sequence is not subject to aliasing effect.

3.1.3 Thermal image analysis

In this study, the infrared thermography technique was introduced to identify the presence of soil cavities by measuring the temporal and spatial variations in the surface temperature of the concrete wall. This technique, which uses measurement and visualization of the surface temperature of the object for analysis and diagnosis using thermal images captured by infrared cameras, has been used for such various scientific and engineering purposes as weather forecasting, ocean temperature monitoring, maintenance and process monitoring, building inspection, and nondestructive testing (Bogue 2013, Al-Kassir *et al*. 2005, Ibarra-Castanedo *et al*. 2013, Usamentiaga *et al*. 2014, Zabin *et al*. 2020). Moreover, infrared thermography was recently integrated with geotechnical engineering applications such detection of a cavity behind a shotcrete wall, structural inspection of concrete retaining walls and shotcrete reinforced slopes, slope instability characterization, and monitoring of rock surface weathering (Guo and Vavilov 2013, Hui and Sun 2012, Lo and Choi 2004, Frodella *et al*. 2014, Wu *et al*. 2005, Cho *et al*. 2016, Yoo 2017, Guerin *et al*. 2019). Such studies have measured the spatial and temporal changes in surface temperature induced by the daily temperature differences between day and night with infrared images, so it can be used as a non-destructive method to evaluate cracks on the concrete surface, stability of fissured rock mass, homogeneity and quality of shotcrete coating and inspect steel bars inside reinforced concrete. In particular, when there is a crack or anomaly on the surface or inside, the surface temperature reacts more sensitively to the external temperature change and the temperature difference with the surrounding area occurs, which is not so significant but can be confirmed through infrared images through refining and processing the measurements.

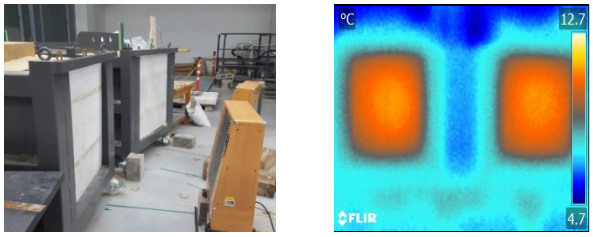

(a) Thermography test (b) Thermal image

Fig. 4 Experimental setup of thermal image analysis for soil cavity detection: Orange colored areas indicate the location of the concrete wall plate

As shown in Fig. 4, halogen heating devices were installed with 1 m spacing in front of the soil chamber to heat the entire surface of the concrete wall for about 12 h. The wall was then allowed to cool to room temperature for 12 h, during which time thermal images were captured every 20 min. The captured images displayed sequential changes in the spatial temperature distribution on the wall surface that occurred during the test.

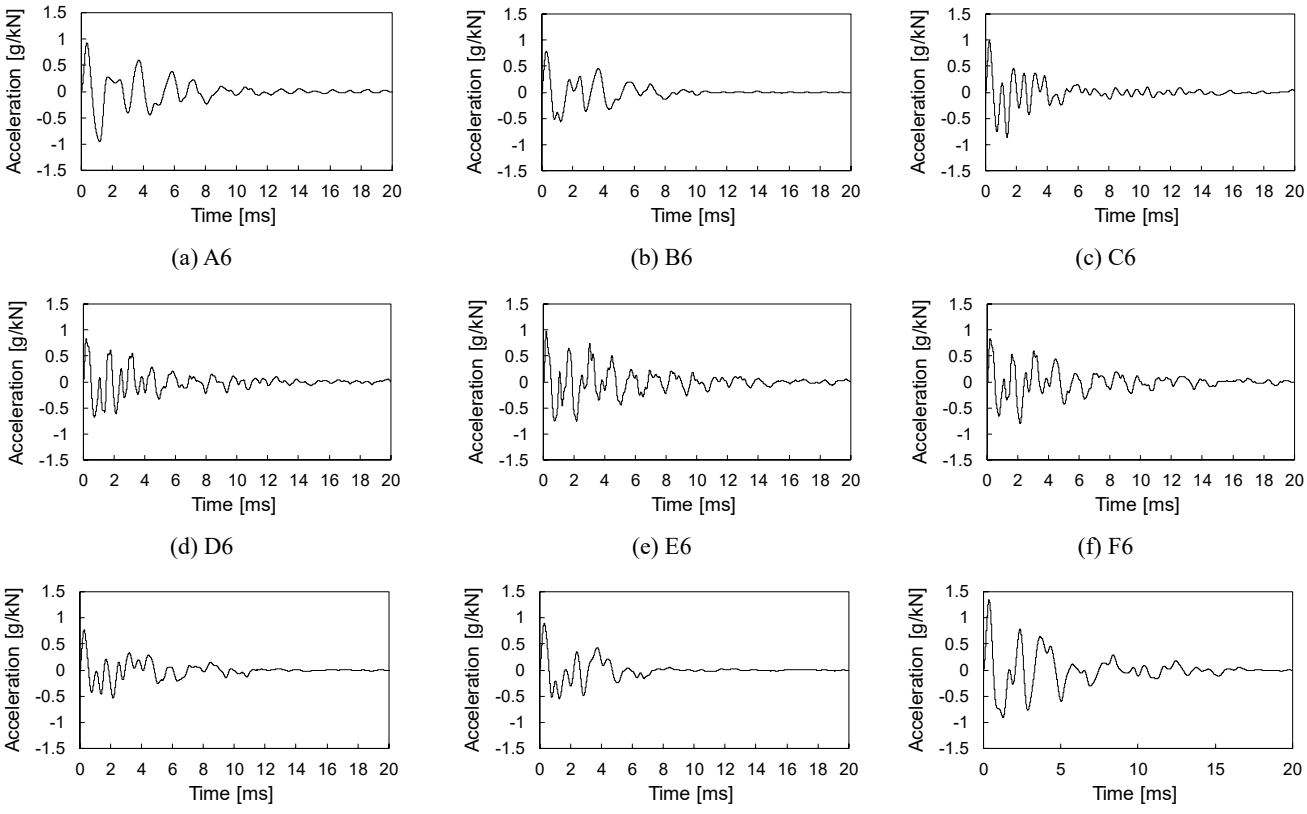

(a) A6 (b) B6 (c) C6

(d) D6 (e) E6 (f) F6

(g) G6 (h) H6 (i) I6

Fig. 5 Measured signals for the sixth row

4. Experimental results

4.1 Elastic waves

Measurements were performed at the 81 grid points on the concrete plate surface, as shown in Fig. 3. The acceleration signals measured at the sixth row (A6–I6), on the horizontal centerline of the cavity, are shown in Fig. 5. To remove the influence of the impact strength, the measured signals were normalized by dividing each measured signal by the maximum force measured at the corresponding measurement points.

For the signals measured at grid points B6, G6, and H6, behind which soils were present, the signal amplitude first decreased significantly and then disappeared after about 10 ms, as shown in Figs. 5(b), 5(g), and 5(h), respectively. In contrast, for those measured at C6, D6, E6, and F6, behind which a cavity was located, the signal amplitude gradually decreased but did not disappear even after about 10 ms, as shown in Figs. 5(c)-(f), respectively. That is, the measured signals showed lower signal attenuation when a cavity was present than that without the cavity. For the signals measured at the grid points A6 and I6, near side edges of the concrete plate, the signal amplitude also gradually decreased but did not disappear even after about 10 ms, as shown in Figs. 5(a) and 5(i).

For all grid points (A1–I6), the measured acceleration signals in the time domain were converted to signals in the frequency domain using FFT. The FFTs of the measured signals in the time domain for the sixth row (A6–I6) are plotted in Fig. 6. In this study, the frequency with the maximum magnitude in the FFT is defined as the predominant frequency. The predominant frequencies for grid points A6, B6, G6, H6, and I6, behind which soils were present, were 0.565 kHz, 0.565 kHz, 0.244 kHz, 0.244 kHz, and 0.488 kHz, as shown in Figs. 6(a), 6(b), 6(g), 6(h), and 6(i), respectively. For grid points C6, D6, E6, and F6, behind which a cavity was located, the predominant frequencies were 1.373 kHz, 0.732 kHz, 0.732 kHz, and 0.732 kHz, respectively, as shown in Figs. 6(c)-(f), respectively. Higher predominant frequencies were observed when a cavity was located behind the concrete plate than those in which only soils were present.

4.2 Thermal imaging

Fig. 7(a) shows the surface temperature distribution in the concrete wall in front of a hemispherical cavity of 40 cm in diameter, which were measured after heating for 12 h. The measured surface temperatures ranged from 14.1°C at the wall boundary to 25.2°C near the center owing to the heat loss around the center-focused unequal heating condition and the heat energy lost near the wall perimeter. The dotted circle in the figure indicates the location of the spherical internal cavity. For comparison, under the same thermal conditions, the surface temperature distribution in the wall was also measured when the cavity was not present, as shown in Fig. 7(b). The thermal images revealed spatial distribution with a minimum temperature of 15.1°C at the wall boundary and a maximum temperature of 27.8°C

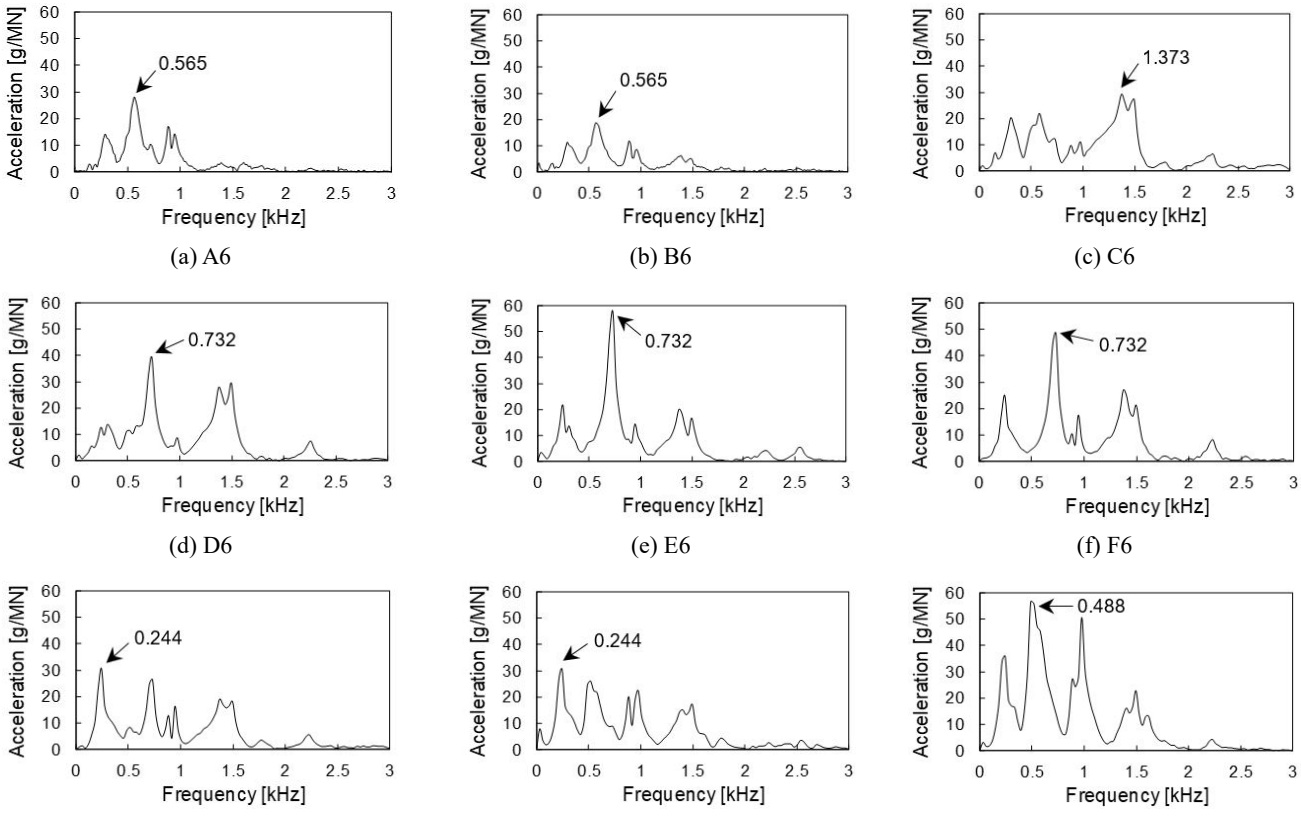

Fig. 6 FFTs of the measured acceleration signals for the sixth row

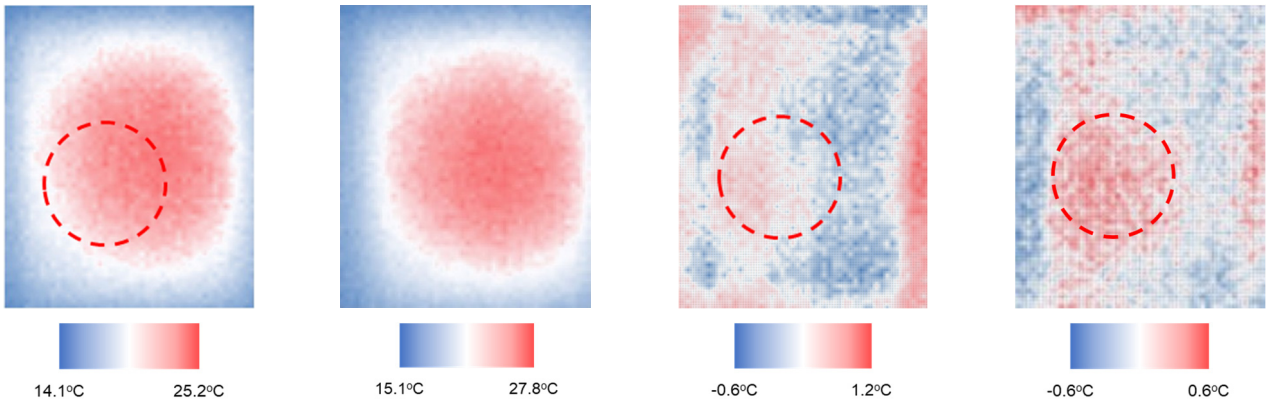

(a) Soil cavity behind the wall when heated for 12 h

(b) No soil cavity behind the wall when heated for 12 h

(c) Normalized surface temperature difference when heated for 12 h

(d) Normalized surface temperature difference when cooled 12 h after heating

Fig. 7 Thermal variations in the surface temperature distribution in the concrete wall plate captured by thermal images: The dotted circles indicate the hemispherical soil cavity behind the wall

near the center, as shown in the figure. Fig. 7(c) shows the computed and normalized differences in spatial temperature distribution with respect to the existence of the internal cavity behind the wall. The temperature differences near the cavity area were at most 1.8°C greater than those of the area without the cavity.

During the cooling, the thermal images of the wall surface were also captured, and the same computations were conducted. The differences in surface temperature depending on the presence or absence of the cavity became more distinct as the cooling period was increased. A consistent thermal trend at about 10°C–12°C was observed during 12 h of cooling at room temperature. Fig. 7(d) shows the computed spatial distribution of the surface temperature difference after 12 h of cooling. The maximum difference was 1.2°C, which is slightly less than the that recorded during the heating sequence. However, the temperature difference near the cavity was more distinct and the shape of the cavity was better defined during the cooling sequence. Whether such temperature differences are sufficient practically for cavity identification in the field is open to debate, but it can be seen that it plays a sufficient role for detecting the cavity in this experimental setup because the currently used infrared camera can measure the surface temperature with a precision of 0.07 degrees.

5. Analyses and discussions

5.1 Signal energy

Elastic wave propagation is affected by geometrical and material attenuations. Concretely, the attenuation of elastic waves is a superimposed effect of the energy loss owing to the radial dissipation of waves and material damping (Finno and Chao 2005). Thus, the geometrical and material characteristics of the concrete plate supporting soils will affect the elastic waves carrying energy and the corresponding the energy of the measured signals.

According to Eq. (1), the total energies of the measured acceleration signals were calculated in the time domain after being normalized by the corresponding impact forces. The variation in total energy of the measured signals at all grid points is plotted in Fig. 8(a). The total energies for the ninth row (A9–I9), which is close to the bottom edge of the concrete plate, were much greater than those for the other rows. Notably, the soil chamber was composed of steel, and the side and bottom edges of the concrete plate were placed on the edges of the soil chamber. The stiffness of steel is much greater than that of concrete (Callister and Rethwisch 2013). Thus, most of the elastic waves were reflected at the interface between the concrete plate and the steel; hence, most of the energy of the elastic waves was trapped within the concrete plate. For this reason, the acceleration signals measured at the ninth row exhibited greater total energy.

Columns A and I are near the side edges of the concrete plates, which were placed at the edges of the soil chamber; therefore, the total energies for columns A and I were greater than those for the other columns. In addition, the total energies were lower when soils were present behind the wall compared with those for columns D and E at rows 5 and 6, where the cavity was present. This is because the energy of the elastic waves was trapped in the concrete plate when the cavity was present. In contrast, the energy of the elastic waves propagating in the concrete was absorbed by the soils when the cavity was absent. The stiffness of sandy soils is much lower than that of concrete. Most of the elastic waves were therefore transmitted into the soils, and the remainder were reflected back into the concrete. Thus, a large amount of the elastic wave energy was absorbed by the soils. To visually inspect the location of the cavity, a contour map for the total energy is illustrated in Fig. 8(b). The total energies were lower when soils were present behind the wall than those near the edges of the concrete and when the cavity was present. Considerably high total energy was recorded near grid point E5. Notably, the center of the actual cavity location was at D6, which is 10 cm to the left and 10 cm to the down from E5. The difference in location between the actual and detected cavities might have occurred because the size of the concrete was not

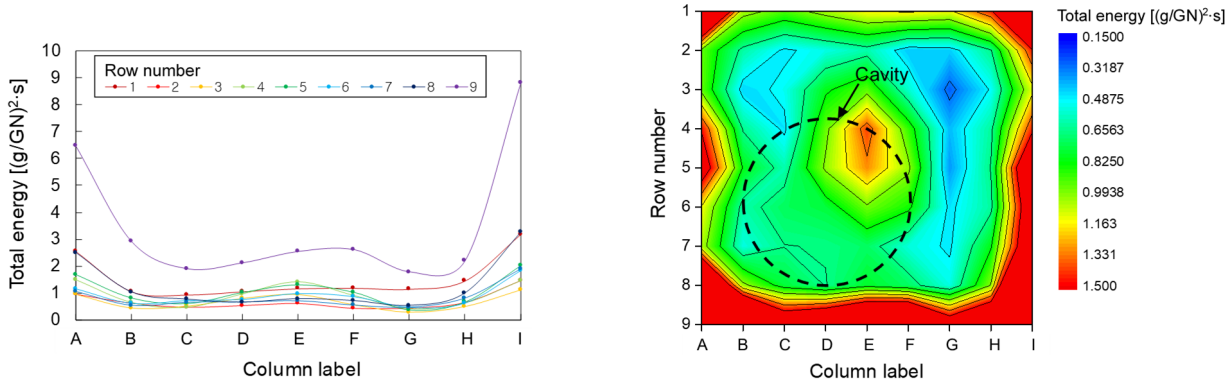

(a) Plotted line (b) Contour map

Fig. 8 Variation in total energy

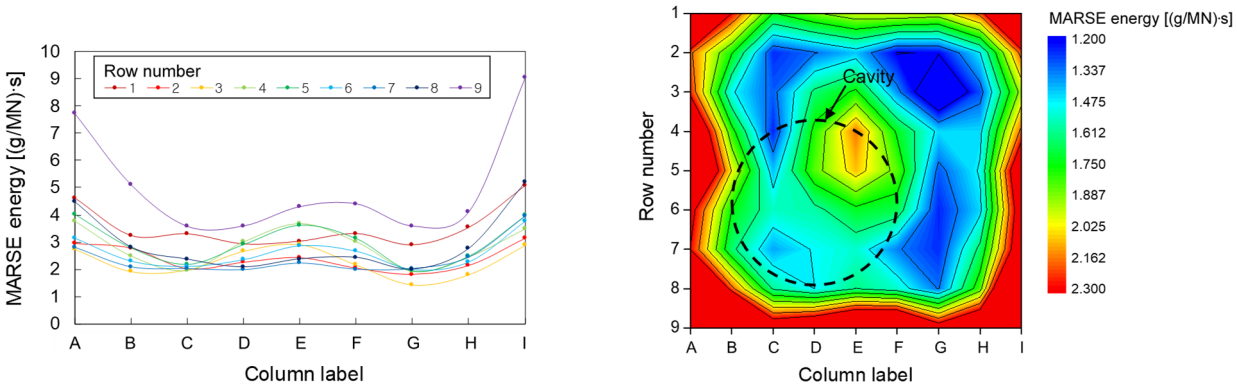

(a) Plotted line (b) Contour map

Fig. 9 Variation in MARSE energy

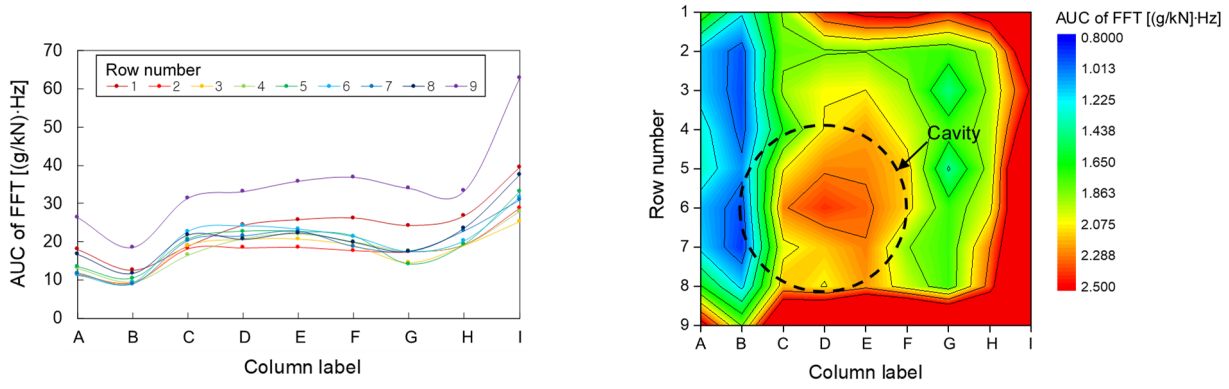

(a) Plotted line (b) Contour map

Fig. 10 Variation in the AUC of FFT

sufficiently large compared with the size of the cavity. This can result in boundary features that affect the propagation energy of the elastic waves. However, the 10 cm difference between the actual and detected location is not significant for field application.

The MARSE energy was also used to detect the cavity location. Because the measured signals showed a very high signal-to-noise ratio (Fig. 5), the MARSE energy was calculated by integrating the absolute value of the measured signals based on Eq. (2) without setting a threshold level. The MARSE energies of the measured acceleration signals in the time domain, which were normalized by the corresponding impact forces, are plotted in Fig. 9(a). The MARSE energies increased significantly near the edges of the concrete plate. However, the energies decreased when soils were present compared with the energies shown for columns D and E at rows 5 and 6, where the cavity was located. The contour map for the MARSE energy, illustrated in Fig. 9(b), shows that the cavity was present near grid point E5, which is similar to that shown in the

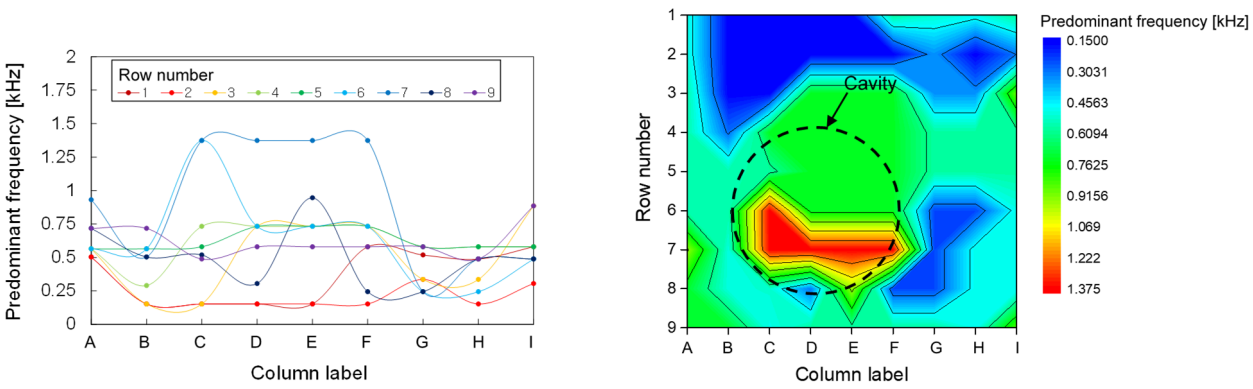

(a) Plotted line (b) Contour map

Fig. 11 Variation in predominant frequency

case of total energy. The MARSE energies were lower for the concrete plate behind which the soils were present compared with those in the presence of the cavity.

In this study, the MARSE energy was calculated as the AUC of the absolute value of the measured signal. In the same manner, the AUC of the FFT was calculated to detect the cavity location. The AUC of the FFT, which is commonly used to characterize signals in NDE techniques (Rizzo *et al*. 2005, Shinoda *et al*. 2013, Tajari 2010), is plotted in Fig. 10(a). The AUC for the ninth row was greater than that for the other rows. In addition, greater AUCs appeared at the grid points (C6–F6), where the cavity was located compared with those reflecting only soils.

Because elastic waves propagating in a medium carry energy, their Fourier transform also includes energy information. Thus, the AUC of FFT was proportional to the MARSE energy. A contour map of the AUC of FFT is illustrated in Fig. 10(b). The detected cavity location is in good agreement with the actual cavity location. In addition, lower AUCs of FFTs appeared for the concrete plate when only soils are present with that in the presence of the cavity, and higher values were recorded near the edges of concrete plate than those measured at other locations.

5.2 Predominant frequency

The FFTs for the acceleration signals normalized by impact forces were obtained; the variation in the predominant frequencies in the FFTs according to the measurement points is plotted in Fig. 11(a). The predominant frequencies for the concrete plate with soils only were lower than those at grid points C6–F6 where the cavity was located. At the interface between the concrete and soils, a portion of elastic waves was reflected, and the remainder was transmitted into the soils. The high-frequency components of the transmitted waves are attenuated easier than low frequency components, and the peak of the Fourier transform shifts to the lower frequency (Santamarina *et al*. 2001). Thus, the predominant frequency for the grid points with soils was lower than that in the presence of the cavity. A contour map of the predominant frequency for all measurement points is illustrated in Fig. 11(b). Higher predominant frequencies appeared near grid point D6, which is the center of the cavity located behind the wall. This result is in good agreement with the actual cavity location.

5.3 Flexibility

The velocity signals were obtained by integrating the acceleration signals with respect to time without normalization by the impact force, and the mobility spectrum was then calculated by dividing the FFT of velocity signals by that of the force signals based on Eq. (3).

For grid points A6–I6, the mobility spectrum within 20 Hz is plotted in Fig. 12 considering that the initial slope of the mobility spectrum within 40 Hz is the flexibility (ASTM C1740 2016). As shown in the figure, the mobility for grid point A6 near the left edge of the concrete plate was the greatest. The mobilities for grid points B6, G6, H6, and I6, where the soils were present behind the wall, were less than those for C6–F6, where the cavity was located. The mobilities were divided by the corresponding frequencies to calculate the initial slope of the mobility (i.e., flexibility). A contour map of the flexibility for all measurement points is illustrated in Fig. 13. Significant flexibility appeared near grid point D6, which is the center of the cavity located behind the wall. In this study, the retaining wall was simulated as a concrete plate supporting soils, which is approximated by an SDOF in which the flexibility (i.e., inverse of the stiffness) is related to the condition of the soils supported by the concrete plate. When soil loss occurs behind the concrete plate, the reaction of the soils is close to

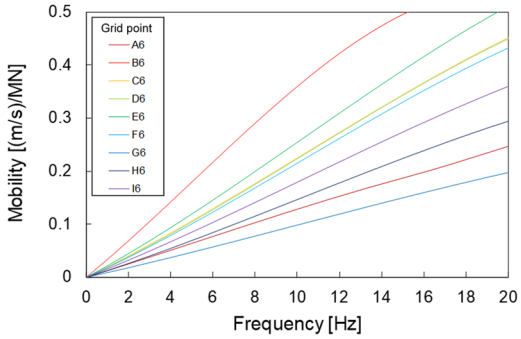

Fig. 12 Mobility spectrum within 20 Hz

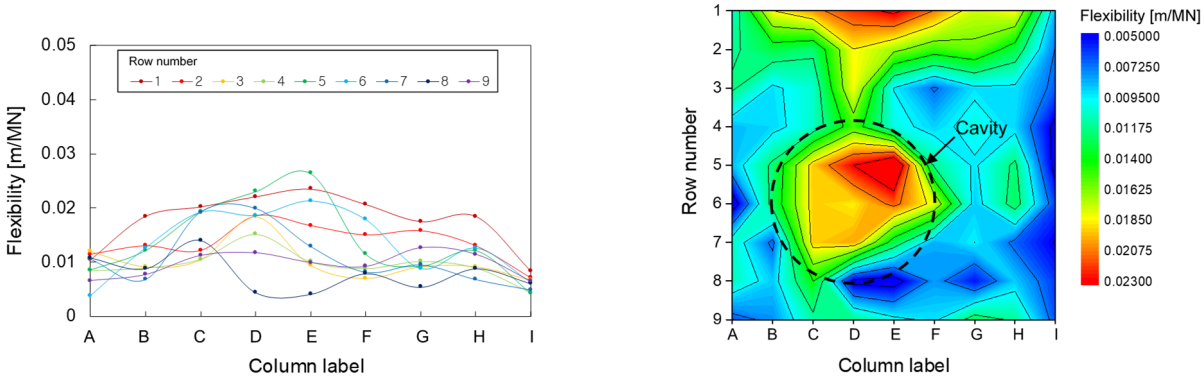

(a) Plotted line (b) Contour map

Fig. 13 Variation in flexibility

zero; hence, the flexibility of the system increases. In good soil condition where no cavity is present, however, the reaction of soils increases, and the flexibility of the system decreases (Nazarian and Reddy 1996). Thus, the grid points where the soil was present behind the wall show lower flexibility than those near the cavity. For the grid points near the edges, the flexibility decreased. The sides of the concrete plate were placed at the edges of the steel soil chamber so that the flexibility of the concrete plate would not be damped by the soils. The top soils in the chamber were free of stress and were not restricted by the soil chamber, which resulted in poor contact between the concrete plate and the soils. Similar effects of the edges on the flexibility condition have also been reported in previous research (McCavitt *et al*. 1992, Nazarian and Reddy 1996).

In this study, the location of the cavity detected using the flexibility was in good agreement with the actual location of the cavity. However, several factors can affect the flexibility (Nazarian *et al*. 1994, Nazarian and Reddy 1996). For example, the flexibility decreases with an increase in the thickness, length, and elastic modulus of the concrete plate and with an increase in the elastic modulus of the soils. If these factors are disregarded, the flexibility can be practically utilized to evaluate the presence of the cavity.

5.4 Thermal imaging

As described in section 4.2, during cooling, the surface temperature of the concrete wall with the internal soil cavity dropped faster than that without the cavity. During cooling sequence, because the air occupying the cavity has a smaller heat capacity than that of the backfilling soils, it loses temperature more quickly. Additionally, the presence of the air-filled zone hampers the flow of heat energy through the cavity.

This difference in temperature is not only related to thermal diffusion caused by external thermal conditions such as heating temperature, heating time, heating area, cooling temperature, cooling time, concrete wall thickness, and the thermal characteristics of the backfilling soils; it is also affected by the experimental environment conditions such as ambient humidity, wind, and other factors. Therefore, quantitative evaluation and the application of this temperature measurement are limited. However, the faster cooling rate and lower temperature near the wall surface behind which the soil cavity was present enables the temperature profile to be used for identifying the presence of a soil cavity behind a thin concrete wall.

5.5 Advantages and limitations

The experimental results showed that elastic waves can effectively be utilized to detect cavity locations by applying various analysis methods such as total energy, MARSE energy, AUC of FFT, predominant frequency, and flexibility in the mobility spectrum. Comparing the results of such analysis methods can increase the reliability of the inspection. Elastic waves provide cavity information at a certain point in a short time with a simple testing method. However, the spatial resolution of the test depends on the number of measurement points, and numerous tests are necessary to investigate a large area. In addition, the boundary condition of the retaining wall affects the accuracy of the elastic wave measurement. Poor coupling between the sensor and the concrete surface owing to concrete roughness, cracking, delamination, weathering, loose particles, and other factors as well as inconsistent coupling can adversely affect the measurement (Kee *et al*. 2012).

Infrared thermography is a non-contact method that provides global visualization of the thermal distribution with high accuracy. Thus, a wide area of the retaining wall can be investigated at the same time regardless of spatial accessibility and coupling issues. However, the main disadvantage of this technique is that the concrete surface must be exposed to sunlight to measure temperature differences between day and night (Staron 1988). In this study, the temperature was easily controlled using heating devices. However, environmental conditions that cause significant temperature differences do not always exist in the field (Washer *et al*. 2009, Avdelidis 2011).

5.6 Description of field applicability

In practice, the infrared thermography is first conducted to scan a global area. Heating and cooling sequences are accomplished by the difference in the temperature between day and night. In the meantime, the variation in the thermal

distribution is monitored to provide thermal image. Then, the points at which a cavity is suspected in the thermal image are investigated precisely using elastic waves. Remarkably, the causes of error in the results of each test are different and independent of each other, which is an advantage of the combined method for facilitating cavity detection.

6. Conclusions

Elastic waves and infrared thermography have been already widely used in structural health monitoring of retaining walls focusing on the evaluation of the structural stability, strength, deformation, and so on. This study tries to propose a complementary hybrid NDT for soil cavity detection at the retaining concrete structures using infrared thermography and elastic wave analyses. The infrared images can be used for the preliminary wide range inspection of soil cavity existence and the elastic wave analyses are applied for confirmation of the targeted spots. Our previous study on the cavity detection has only been carried out on pavement models using the mobility spectrum. However, in this study, elastic waves were analyzed using signal energies, including total and MARSE energy, AUC of FFT, and predominant frequency besides the mobility spectrum to provide better reliability and validity of results.

In experiments, a small-scale model of a retaining wall, which consisted of a concrete plate and soils, was prepared for the experiments. A hemispherical cavity was simulated behind the concrete plate, and a total of 81 measurement points were set 10 cm apart on the concrete plate. The generation and detection of elastic waves were accomplished by using an instrument hammer and an accelerometer, respectively. The measured signals were displayed on an oscilloscope and were recorded on a computer. The signal energy, predominant frequency, and flexibility in the mobility spectrum of the measured signals were analyzed to evaluate the cavity location. To monitor the responses to thermal change, the concrete plate was heated for 12 h using halogen heaters and was then cooled for 12 h at room temperature. The thermal images were captured during both heating and cooling sequences.

The experimental results of the elastic wave measurements showed that the signal energy of measured signals, including total and MARSE energies and the AUC of FFT, was greater when the cavity was present behind the concrete plate than that when only soils were present. This occurred because most of elastic waves were trapped within the concrete plate when the cavity was present behind it. Elastic waves are transmitted into the soils, and the propagation energy was absorbed by the soils present behind the concrete plate without the cavity owing to differences in the stiffness between the concrete and the soils. Notably, the stiffness of soils is much lower than that of concrete. In addition, the presence of the cavity resulted in increased predominant frequency because the high-frequency components of the signals are attenuated easier than low frequency components. Furthermore, the presence of the cavity increased the flexibility in the mobility spectrum, whereas the flexibility decreased when only soils were present behind the concrete plate owing to variation in the stiffness of the concrete–soil composite system. Notably, the local stiffness of the concrete where the cavity is present was smaller than that of the concrete supported by soils. That is, the presence of the cavity increased the flexibility of the concrete plate. The cavity location detected by signal energy, predominant frequency, and flexibility was in good agreement with the actual defect location.

In the heating sequence, the temperature near the wall boundary was lower than that near the center of the wall owing to the unequal and center-concentrated heating condition and the heat energy loss near the soil chamber boundary. Nevertheless, the cavity was identified by the temperature difference between the cavity area and non-cavity area owing to the differences in the thermal characteristics of soil and air. Lower temperature was observed at the cavity area, which was more distinct during the cooling sequence. Notably, the heat capacity of the air occupying the cavity is much smaller than that of the backfilling soil and affected the thermal energy flow through the cavity. Thus, the surface area in the presence of the cavity was more sensitive to the temperature drop compared with that in the non-cavity area.

Elastic wave methods are preferred for identifying the presence of a cavity point by point owing to their rapid testing procedure and reliability in the analysis results. Infrared thermography is a non-contact method suitable for inspecting wide areas regardless of the accessibility and sensor-coupling problem. For more reliable soil cavity detection using NDT techniques, this study suggests the combined nondestructive testing method using thermography first followed by confirmation of the results through elastic wave reflection.

Acknowledgments

This work was supported by the National Research Foundation of Korea (NRF) grant funded by the Korea government (MSIT) (No. 2019R1A2C1088527).

References

Al-Kassir, A.R., Fernandez, J., Tinaut, F. and Castro, F. (2005), "Thermographic study of energetic installations", *Appl. Therm. Eng.*, **25**(2-3), 183-190. https://doi.org/10.1016/j.applthermaleng.2004.06.013

ASTM C1740 (2016), Standard Practice for Evaluating the Condition of Concrete Plates Using the Impulse-response Method, ASTM International, West Conshohocken, PA, USA.

Avdelidis, N.P., Gan, T.H., Ibarra-Castanedo, C. and Maldague, X.P.V. (2011), "Infrared thermography as a nondestructive tool for materials characterisation and assessment", *Proceedings of SPIE*, Orlando, FL, USA, May.

Bogue, R. (2013), "Sensors for condition monitoring: A review of technologies and applications", *Sens. Rev.*, **33**(4), 295-299. https://doi.org/10.1108/SR-05-2013-675

Brooks, H. (2010), *Basics of Retaining Wall Design*: *A Design Guide for Earth Retaining Structure*, BHA Publication, Inc., Corona del Mar, CA, USA.

Callister, W.D. and Rethwisch, D.G. (2007), *Materials Science*

and Engineering: *An Introduction*, John Wiley & Sons, Inc., Hoboken, NJ, USA.

Ching, F.D.K. and Winkel, S.R. (2018), *Building Codes Illustrated*: *A Guide to Understanding the 2018 International Building Code*, John Wiley & Sons, Inc., Hoboken, NJ, USA.

Cho, N.J., Cha, W. and Kim, H.K. (2016), "Non-destructive detection of underground cavities using thermal images", *Electron*. *J. Geotech*. *Eng*., **21**(16), 5465-5476.

Choudhury, D. and Chatterjee, S. (2006), "Dynamic active earth pressure on retaining structures", *Sadhana*, **31**(6), 721-730.

Davis, A.G. (2003), "The nondestructive impulse response test in North America: 1985-2001", *NDT & E Int*., **36**(4), 185-193.

Davis, A.G. and Dunn, C.S. (1974), "From theory to field experience with the non-destructive vibration testing of piles", *Proceedings of the Institution of Civil Engineers*, **57**(4), 571-593. https://doi.org/10.1680/iicep.1974.3895

Embacher, R., Schultz, A. and Snyder, M. (2001), "Condition and durability of segmental concrete block retaining walls along roadways in Minnesota", Research Report No. MN/RC-2001-16; Minnesota Department of Transportation.

Finno, R.J. and Chao, H. (2005), "Guided waves in embedded concrete pile", *J. Geotech*. *Geoenviron*., **131**(1), 11-19. https://doi.org/10.1061/(ASCE)1090-0241(2005)131:1(11)

Frodella, W., Morelli, S., Gigli, G. and Casagli, N. (2014), "Contribution of infrared thermography to the slope instability characterization", *Proceedings of World Landslide Forum*, Beijing, China, June.

Gazetas, G. (1983), "Analysis of machine foundation vibration: State of the art", *Soil Dyn*. *Earthq*. *Eng*., **2**(1), 1-42. https://doi.org/10.1016/0261-7277(83)90025-6

Grandt, A.F. (2004), *Fundamentals of Structural Integrity*: *Damage Tolerant Design and Nondestructive Evaluation*, John Wiley & Sons, Inc., Hoboken, NJ, USA.

Guerin, A., Jaboyedoff, M., Collins, B.D., Derron, M.H., Stock, G.M., Matasci, B., Lefeuvre, C. and Podladchikov, Y.Y. (2019), "Detection of rock bridges by infrared thermal imaging and modeling". *Sci*. *Rep*., **9**(1), 1-19. https://doi.org/10.1038/s41598-019-49336-1

Guo, X. and Vavilov, V. (2013), "Crack detection in aluminum parts by using ultrasound-excited infrared thermography", *Infrared Phys*. *Technol*., **61**, 149-156. https://doi.org/10.1016/j.infrared.2013.08.003

Hugenschmidt, J. and Kalogeropoulos, A. (2009), "The inspection of retaining walls using GPR", *J. Appl*. *Geophy*., **67**(4), 335-344. https://doi.org/10.1016/j.jappgeo.2008.09.001

Hui, T.H.H. and Sun, H.W. (2005), "Trial application of thermal infra-red image and seismic sympathetic vibration techniques for slope investigation", GEO Technical Note No. TN1/200; Civil Engineering and Development Department, The Government of the Hong Kong Special Administrative Region.

Ibarra-Castanedo, C., Tarpani, J.R. and Maldague, X.P. (2013), "Nondestructive testing with thermography", *Eur*. *J. Phys*., **34**(6), S91. https://doi.org/10.1088/0143-0807/34/6/S91

KDS 14 20 72 (2021), Korean Design Standard - Design Standard for Concrete Wall, Korea Construction Standards Center, Gyeonggi-do, Republic of Korea.

Kee, S.H., Oh, T., Popovics, J.S., Arndt, R.W. and Zhu, J. (2012), "Nondestructive bridge deck testing with air-coupled impact-echo and infrared thermography", *J. Bridge Eng*., **17**(6), 928-939. https://doi.org/10.1061/(ASCE)BE.1943-5592.0000350

Koerner, R.M. and Soong, T.Y. (2001), "Geosynthetic reinforced segmental retaining walls", *Geotext*. *Geomembr*., **19**(6), 359-386. https://doi.org/10.1016/S0266-1144(01)00012-7

Lin, C.S., Chen, S.H., Chang, C.M. and Shen, T.W. (2019), "Crack detection on a retaining wall with an innovative, ensemble learning method in a dynamic imaging system", *Sensors*, **14**, 12305-12348. https://doi.org/10.3390/s19214784

Lo, T.Y. and Choi, K.T.W. (2004), "Building defects diagnosis by infrared thermography", *Struct*. *Surv*., **22**(5), 259-263. https://doi.org/10.1108/02630800410571571

McCavitt, N., Yates, M.R. and Forde, M.C. (1992), "Dynamic stiffness analysis of concrete pavement slabs", *J. Transp*. *Eng*., **118**(4), 540-556. https://doi.org/10.1061/(ASCE)0733-947X(1992)118:4(540)

Nazarian, S. and Reddy, S. (1996), "Study of parameters affecting impulse response method", *J. Transp*. *Eng*., **122**(4), 308-315. https://doi.org/10.1061/(ASCE)0733-947X(1996)122:4(308)

Nazarian, S., Reddy, S. and Baker, M. (1994), "Determination of voids under rigid pavements using impulse response method", In: Nondestructive Testing of Pavements and Backcalculation of Moduli: Second Volume, ed. Bush, A., Von, H.Q. and Baladi, G., ASTM International, West Conshohocken, PA, USA, pp. 473-487. https://doi.org/10.1520/STP18165S

Obe, R.K.D., Brito, J., Mangabhai, R. and Lye, C.Q. (2017), *Sustainable Construction Materials*: *Copper Slag*, Woodhead Publishing, Cambridge, MA, USA.

Ottosen, N.S., Ristinmaa, M. and Davis, A.G. (2004), "Theoretical interpretation of impulse response tests of embedded concrete structures", *J. Eng*. *Mech*., **130**(9), 1062-1071. https://doi.org/10.1061/(ASCE)0733-9399(2004)130:9(1062)

Padhye, R.D. and Ullagaddi, P.B. (2008), "Case study of failure of a R.C.C. counterfort retaining wall", *Proceedings of the 6th International Conference on Case Histories in Geotechnical Engineering*, Arlington, VA, USA, August.

Papazafeiropoulos, G., Psarropoulos, P.N. and Tsompanakis, Y. (2009), "Retaining wall-soil-structure interaction effects due to seismic excitation", *Proceedings of the 17th International Coference on Soil Mechanics & Geotechnical Engineering*, Alexandria, Egypt, October.

Park, J.Y., Jang, E., Kim, H.J. and Ihm, M.H. (2017), "Classification of ground subsidence factors for prediction of ground subsidence risk (GSR)", *J. Eng*. *Geol*., **27**(2), 153-164. https://doi.org/10.9720/kseg.2017.2.153 [In Korean]

Prasad, S.K., Jagadeesh, N.M. and Yadunandan, C.N. (2014), "Case studies on failure of retaining walls", *i-Manager's J. Civil Eng*., **3**(2), 29-34. https://doi.org/10.26634/jste.3.2.3019.

Rainieri, C., Fabbrocino, G. and Magistris, F.S. (2013), "An integrated seismic monitoring system for a full-scale embedded retaining wall", *Geotech*. *Test*. *J*., **36**(1), 1-14. https://doi.org/10.1520/GTJ20120067

Rizzo, P., Bartoli, I., di Scalea., F.L., Coccia, S. and Fateh, M. (2005), "High-speed defect detection in rails by non-contact guided ultrasonic testing", *Proceedings of SPIE - The International Society for Optical Engineering*, San Diego, CA, USA, December.

Santamarina, J.C., Klein, K.A. and Fam, M.A. (2001), *Soils and Waves*, John Wiley & Sons, Inc., Hoboken, NJ, USA.

Seo, H.J., Zhao, Y. and Wang, J. (2019), "Monitoring of retaining structures on an open excavation site with 3D laser scanning", *International Conference on Smart Infrastructure and Construction 2019* (*ICSIC*) *Driving Data-informed Decision-making*, Churchill College, Cambridge, UK, July.

Shinoda, M., Nakajima, S., Abe, K., Ehara, T. and Kubota, Y. (2013), "Stability inspection method for existing retaining walls", *Q*. *Rep*. *RTRI*, **54**(3), 159-165. https://doi.org/10.2219/rtriqr.54.159

Staron, D.L. (1988), "Concrete deterioration inspection system for extending the operating life of nuclear power plants", Ph.D. Dissertation, Virginia Polytechnic Institute and State University, Blacksburg, VA, USA.

Tajari, M. (2010), "Use of microphone directivity for the localization of sound sources", Ph.D. Dissertation; University of Pittsburgh, Pittsburgh, PA, USA.

Unnþórsson, R. (2013), "Hit detection and determination in ae

bursts", In: *Acoustic Emission*: *Research and Aapplications*, (ed. Sikorski, W.), IntechOpen, London, UK, pp. 1-19.
Usamentiaga, R., Venegas, P., Guerediaga, J., Vega, L., Molleda, J. and Bulnes, F.G. (2014), "Infrared thermography for temperature measurement and non-destructive testing", *Sensors*, **14**, 12305-12348.
Veletsos, A.S. and Younan, A.H. (1994), "Dynamic modeling and response of soil-wall systems", *J. Geotech. Geoenviron.*, **120**(12), 2155-2179. https://doi.org/10.1061/(ASCE)0733-9410(1994)120:12(2155)
Washer, G., Fenwick, R., Bolleni, N. and Harper, J. (2009), "Effects of environmental variables on infrared imaging of subsurface features of concrete bridges", *Transp. Res. Rec.*, **2108**(1), 107-114. https://doi.org/10.3141/2108-12
Wu, J.H., Lin, H.M., Lee, D.H. and Fang, S.C. (2005), "Integrity assessment of rock mass behind the shotcreted slope using thermography", *Eng. Geol.*, **80**(1), 164-173. https://doi.org/10.1016/j.enggeo.2005.04.005
Yang, H., Koopialipoor, M., Armaghani, D.J., Gordan, B., Khorami, M. and Tahir, M.M. (2019), "Intelligent design of retaining wall structures under dynamic conditions", *Steel Compos. Struct., Int. J.*, **31**(6), 629-640. http://dx.doi.org/10.12989/scs.2019.31.6.629
Yoo, S. (2017), "Engineering application of infrared image for stability evaluation on concrete retaining wall", Master's Thesis; Kookmin University, Seoul, Korea.
Yoo, C. and Jung, H.Y. (2006), "Case history of geosynthetic reinforced segmental retaining wall failure", *J. Geotech. Geoenviron.*, **132**(12), 1538-1548. https://doi.org/10.1061/(ASCE)1090-0241(2006)132:12(1538)
Zabin, A., Khalil, B., Ali, T., Abdalla, J.A. and Elaksher, A. (2020), "A semi-automated method for integrating textural and material data into as-built BIM using TIS", *Adv. Comput. Des., Int. J.*, **5**(2), 127-146. http://dx.doi.org/10.12989/acd.2020.5.2.127

CC